EXCITED-STATE STRUCTURE AND ISOMERIZATION DYNAMICS OF THE RETINAL CHROMOPHORE IN RHODOPSIN FROM RESONANCE RAMAN INTENSITIES

GLEN R. LOPPNOW AND RICHARD A. MATHIES
Department of Chemistry, University of California, Berkeley, California 94720

ABSTRACT Resonance Raman excitation profiles have been measured for the bovine visual pigment rhodopsin using excitation wavelengths ranging from 457.9 to 647.1 nm. A complete Franck-Condon analysis of the absorption spectrum and resonance Raman excitation profiles has been performed using an excited-state, time-dependent wavepacket propagation technique. This has enabled us to determine the change in geometry upon electronic excitation of rhodopsin's 11-*cis*-retinal protonated Schiff base chromophore along 25 normal coordinates. Intense low-frequency Raman lines are observed at 98, 135, 249, 262, 336, and 461 cm^{-1} whose intensities provide quantitative, mode-specific information about the excited-state torsional deformations that lead to isomerization. The dominant contribution to the width of the absorption band in rhodopsin results from Franck-Condon progressions in the 1,549 cm^{-1} ethylenic normal mode. The lack of vibronic structure in the absorption spectrum is shown to be caused by extensive progressions in low-frequency torsional modes and a large homogeneous linewidth (170 cm^{-1} half-width) together with thermal population of low-frequency modes and inhomogeneous site distribution effects. The resonance Raman cross-sections of rhodopsin are unusually weak because the excited-state wavepacket moves rapidly (~35 fs) and permanently away from the Franck-Condon geometry along skeletal stretching and torsional coordinates.

INTRODUCTION

Rhodopsin, the light-sensitive visual pigment found in the retinal rod cells of vertebrates, is responsible for scotopic or night vision. It is a 41,000-D protein containing an 11-*cis*-retinal prosthetic group (Scheme I) bound to lysine 296 as a protonated Schiff base (1). The primary event in vision is *cis-trans* photoisomerization about the $C_{11}=C_{12}$ bond (2). The structure of the primary photoproduct, bathorhodopsin, has been studied extensively with resonance Raman (3–5) and FTIR spectroscopy (6–8), and is thought to be distorted all-*trans*. Picosecond absorption (9, 10), Raman (11), and fluorescence (12) studies indicate that the isomerization occurs on a picosecond timescale. INDO calculations predict that 2 ps is a reasonable time for the appearance of ground-state bathorhodopsin (13). Several models have been proposed for the mechanism of this *cis-trans* isomerization (13–16), but more data are needed to quantitatively determine how this rapid isomerization process occurs.

Resonance Raman intensities provide detailed information about excited-state structure and dynamics on an extremely fast timescale (17). The intensity of each vibrational line in a resonance Raman experiment directly reflects the geometry change between the ground and excited electronic states along that normal coordinate. Self-consistent analysis of the absorption spectrum and the resonance Raman excitation profiles can also yield such information as the homogeneous and inhomogeneous linewidths. In this way, excited-state structure and dynamics have been studied in a wide range of molecules, including bacteriorhodopsin (18), stilbene (19), cytochrome *c* (20), and nucleic acids (21).

The purpose of this paper is to use resonance Raman intensities to examine the excited-state structure and isomerization dynamics of rhodopsin. Specifically, we will analyze resonance Raman excitation profiles to develop a model for the multidimensional excited-state potential surface of the retinal prosthetic group, and to set limits on the excited-state isomerization and relaxation times. The resonance Raman intensities of 25 vibrational modes were measured as a function of excitation wavelength. These excitation profiles were analyzed to determine excited-state geometry changes for each of the observed normal modes and to define the contributions of homogeneous (single molecule) and inhomogeneous (ensemble) broadening to the overall absorption bandshape. An important result of this study is the observation of intense low-frequency skeletal torsional modes whose Franck-Condon progressions contribute significantly to the homogeneous absorption bandshape.

Address correspondence and reprint requests to Dr. Richard A. Mathies.

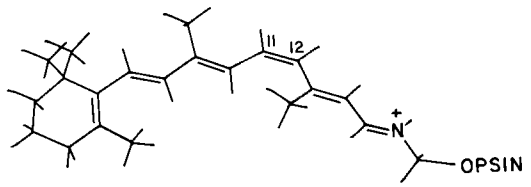

Scheme I

MATERIALS AND METHODS

Experimental

Frozen bovine retinas were purchased from J. A. Lawson (Lincoln, NE), and the rod outer segments were isolated by a sucrose flotation method (22). The rod outer segments were lysed in water and solubilized in 5% Ammonyx-LO (Onyx Chemical Co., Jersey City, NJ). The resulting rhodopsin solution was purified by hydroxylapatite chromatography (22) and concentrated in Amicon membrane cones to 15–30 μM. Typical yields were 750–1,500 nmol rhodopsin per 100 retinas.

Room-temperature, rapid-flow resonance Raman spectra of rhodopsin were obtained with 10–15-ml samples having an absorbance of 0.8–1.5 OD/cm at 500 nm (100 mM phosphate buffer, <10 mM $NH_2OH \cdot HCl$, <1% Ammonyx-LO, pH 6.8–7.0) and containing 0.2–0.6 M potassium nitrate as an internal intensity standard. Addition of potassium nitrate had no noticeable effect on the absorption or resonance Raman spectra of rhodopsin. Raman scattering was excited by spherically focusing the laser beam in the 0.8-mm diameter capillary containing the flowing rhodopsin solution. Laser excitation was obtained with Kr and Ar ion lasers (Spectra-Physics, Mountain View, CA, models 171 and 2020). Multichannel detection of the Raman scattering was accomplished with a cooled intensified vidicon detector (PAR 1205A/1205D) coupled to a double spectrograph. Single-channel photon-counting spectra were obtained with a double monochromator system (22). Spectral slit widths were 5.0–6.0 cm^{-1}. The laser power (300–600 μW), flow rate (300–400 cm/s), and beam waist (10 μm) were chosen to minimize the effects of photolysis on the Raman spectra (photoalteration parameter F~0.1, reference 23). The actual bulk photolysis rate was determined by measuring the absorption spectrum of the sample after each Raman scan. The multichannel Raman spectrometer was calibrated using cyclohexene and dicyclopentadiene as external standards. Frequencies are accurate to ±4 cm^{-1}.

Raman data collection was performed with a PDP 11/23 computer. Reported spectra are the sum of three to nine scans. All spectra were corrected for the wavelength dependence of the spectrometer efficiency using a standard lamp. Fluorescence backgrounds were removed by subtracting a quartic polynomial, and the spectra were digitally smoothed using a three-point sliding average. The integrated intensities of the rhodopsin lines relative to the 1,049 cm^{-1} nitrate line were obtained by fitting regions of the spectrum to sums of Lorentzian peaks convoluted with a triangular slit function. The relative intensities of the rhodopsin lines were then corrected for self absorption using a 0.4-mm path length. The differential self-absorption correction between the nitrate line and any rhodopsin fundamental was no more than 15%. Absolute Raman cross-sections were found from the relative integrated intensities using:

$$\sigma_{RHO} = \sigma_{NO_3} \frac{\left(\frac{1+2\rho}{1+\rho}\right)_{RHO} [NO_3]\, I_{RHO}}{\left(\frac{1+2\rho}{1+\rho}\right)_{NO_3} [RHO]\, I_{NO_3}}, \quad (1)$$

where ρ is the depolarization ratio of the scattered light ($\rho_{NO_3} = 0.04$ and $\rho_{RHO} = 0.33$). Nitrate concentrations were determined by comparing the nitrate scattering of the bleached rhodopsin sample with that of a series of standard nitrate solutions. The average concentration of rhodopsin in each experiment was found by interpolation of the A_{500} values measured before and after each rhodopsin Raman scan.

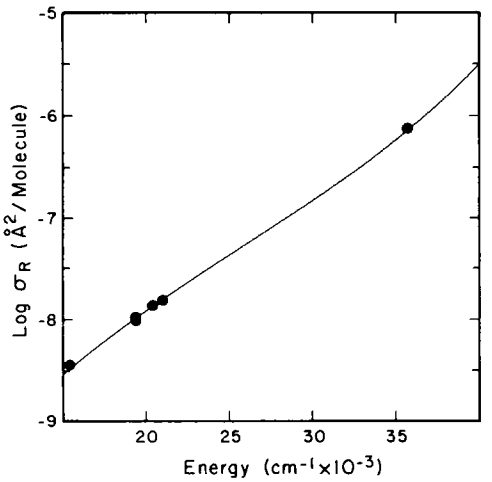

FIGURE 1 A-term fit to the nitrate cross-sections. The solid line was calculated with Eq. 2 using $K = 8.393 \times 10^{-12}$ Å^2/molecule, $\nu_e = 51{,}940$ cm^{-1}, and $C = 5.2 \times 10^{-5}$ cm^2. The estimated errors are on the order of the point size.

Absolute Raman cross-sections of nitrate were obtained by comparison with known values for sulfate. The relative intensities of the 1,049 cm^{-1} nitrate line to the 981 cm^{-1} sulfate line were measured by recording Raman spectra of 0.2 M nitrate and 0.2 M sulfate. The ratios (sulfate:nitrate) were 0.89 ± 0.02, 0.90 ± 0.01, 0.91 ± 0.02, and 1.10 ± 0.05 at 476.5, 488, 514.5, and 647.1 nm. These ratios were converted to absolute cross sections using Eq. 1, where $\rho_{SO_4} = 0.04$, and $\sigma_{SO_4} = 137$, 124, 99.3, and 39.5 μbarns at 476.5, 488, 514.5, and 647 nm, respectively (18).[1] The resulting nitrate cross-sections were 154 ± 15, 138 ± 14, 109 ± 11, and 36 ± 4 μbarns at 476.5, 488, 514.5, and 647.1 nm, respectively. The nitrate data were fit to Eq. 2 using these four points plus cross-sections of 7,340 ± 1,470 μbarns at 280 nm and 101 ± 20 μbarns at 514.5 nm from reference 26.

$$\sigma_R = \frac{8\pi}{3}\left(\frac{1+2\rho}{1+\rho}\right) K \nu_e \nu^3 \left[\frac{\nu_e^2 + \nu_0^2}{(\nu_e^2 - \nu_0^2)^2} + C\right]^2. \quad (2)$$

In this equation, ν_e is the resonant electronic energy, ν is the scattered photon energy, ν_0 is the incident photon energy, K is a fitting constant, and C gives the contribution from background electronic states (27). The data, A-term fit, and fitting parameters are presented in Fig. 1. We used the calculated nitrate cross-sections of 159 ± 21, 140 ± 18, 106 ± 14, 64 ± 8, and 34 ± 4 μbarns at 476.5, 488, 514.5, 568, and 647.1 nm, respectively, in the determination of absolute cross-sections for rhodopsin.

Theory

The resonance Raman and absorption cross-sections in the Condon approximation can be written using the time-dependent formalism of Lee

[1]The sulfate cross-sections of reference 18 were referenced to a benzene cross-section of 224 μbarns (1 μbarn = 1×10^{-14} Å^2) at 514.5 nm (24). More detailed measurements now give a value for the cross-section of benzene at 514.5 nm as 258 μbarns (25). Therefore, we have rescaled the sulfate cross-section of reference 18 at 514.5 nm from 93.0 μbarns to 99.3 μbarns. The reported sulfate cross-sections are taken from the A-term fit of data from reference 18. All values are ±10%.

and Heller (28) as

$$\sigma_R = \frac{8\pi E_S^3 E_L e^4 M^4}{9\hbar^6 c^4} \cdot \sum_i B_i \left| \int_0^\infty \langle f|i(t)\rangle\, e^{i(E_L+\epsilon_i)t/\hbar}\, e^{-\Gamma^2 t^2/\hbar^2}\, dt \right|^2 \quad (3)$$

$$\sigma_A = \frac{4\pi e^2 M^2 E_L}{6\hbar^2 c n} \cdot \sum_i B_i \int_{-\infty}^{\infty} \langle i|i(t)\rangle\, e^{i(E_L+\epsilon_i)t/\hbar}\, e^{-\Gamma^2 t^2/\hbar^2}\, dt, \quad (4)$$

where $|i\rangle$ and $|f\rangle$ are the initial and final vibrational wavefunctions in the Raman process, ϵ_i is the energy of the initial vibrational level, E_L and E_S are the energies of the incident and scattered photons, Γ is a Gaussian homogeneous linewidth function, and B_i is the normalized Boltzmann factor for state i.[2] In this expression, $|i(t)\rangle = e^{-iHt/\hbar}|i\rangle$ is the initial ground state vibrational wavefunction propagated on the excited-state potential surface. A one-dimensional example of this wavepacket propagation is presented in Fig. 2. The ground state vibrational wavefunction, $|i\rangle$, is carried to the excited-state surface by the incident photon. Because it is not an eigenstate of the excited-stated Hamiltonian, the wavepacket propagates on the excited-state surface. The time-dependent overlap with the initial state, $\langle i|i(t)\rangle$, determines the absorption spectrum, whereas the overlap with the final state, $\langle f|i(t)\rangle$, generates the Raman excitation profiles. The Fourier transforms of these overlaps give the theoretical absorption spectrum and Raman excitation profiles. In the separable multimode case, the multidimensional absorption overlap is the product of the one-dimensional overlaps $\langle i|i(t)\rangle$ for each normal mode. The multimode Raman overlap in Eq. 3 is the product of $\langle f|i(t)\rangle$ in the Raman active mode and $\langle i|i(t)\rangle$ in all other modes. The implementation of these equations has been described in detail (17).

In our treatment, each high-frequency vibrational degree of freedom is described by its frequency and a displacement Δ, in dimensionless normal coordinates, between ground and excited-state harmonic potential surface minima (see Fig. 2). We are assuming that anharmonicities, Duschinsky rotation of the excited-state normal coordinates, and frequency changes are less important than the potential surface origin displacement. This has been shown to be a reasonable initial assumption for high-frequency modes in the vibronic analysis of polyenes (29).

Vibrations below ~500 cm^{-1} can be modeled in two equivalent ways. The first approach is to use a bound harmonic excited-state surface with no excited-state frequency changes. This model is likely to be inaccurate at long propagation times because the excited-state surfaces of these coordinates are expected to have large frequency changes and anharmonicities which would alter $|i(t)\rangle$ at long times. However, as will be shown later, the Raman cross-sections indicate that rhodopsin scatters in the "short time limit," which means that the multimode Raman overlap $\langle f|i(t)\rangle$ decays very rapidly (~35 fs). Because the propagating wavepacket only samples a small portion of the excited-state surface along low-frequency modes during this short time, only the slope of the excited-state potential surface in the Franck-Condon region is important for the analysis. Thus, it is equivalent to model the excited-state surface for low-frequency modes as a linear dissociative potential. For a harmonic excited-state surface, the relationship between Δ and the excited-state slope in the Franck-Condon region is $\beta/\hbar = \Delta\omega$, where $\beta/\hbar$ is the excited-state slope in cm^{-1} and ω is the excited-state frequency. In the short-time limit the second derivative of the excited-state potential surface is less important than the slope in determining the dynamics. Hence, anharmonicities and frequency changes in the excited state need not be explicitly considered.

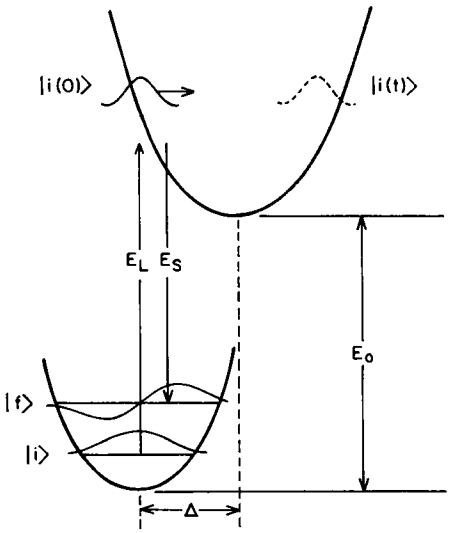

FIGURE 2 The time-dependent picture of resonance Raman scattering for a bound harmonic excited-state surface. The change of the equilibrium geometry upon electronic excitation is denoted by Δ. E_L and E_S are the incident and scattered photon energies, and E_0 is the energy gap between potential minima. The initial and final vibrational wavefunctions in the Raman process are $|i\rangle$ and $|f\rangle$. The excited-state wavepacket $|i(t)\rangle = e^{-iHt/\hbar}|i\rangle$ is the initial ground-state Gaussian vibrational wavefunction propagated on the excited-state potential surface.

Measurement of the Raman excitation profiles permits the differentiation of homogeneous and inhomogeneous contributions to the absorption bandshape (17). The homogeneous absorption band arises from Franck-Condon transitions in explicit modes, each of which is broadened by the homogeneous linewidth. As the homogeneous lineshape becomes broader, either through Franck-Condon or lifetime effects, the excitation profiles and the absorption spectrum become diffuse. In addition, the resonance Raman cross-sections are strongly reduced as the homogeneous width is increased. Thus, the resonance Raman cross-sections provide a sensitive probe of the overall homogeneous width. In the case of rhodopsin, the absorption lineshape requires that the homogeneous damping function in Eqs. 3 and 4 be a Gaussian of the form $e^{-\Gamma^2 t^2/\hbar^2}$.

In condensed phase we must also include inhomogeneous or 'site' distribution effects, which have been modeled as a Gaussian distribution of zero–zero energies with standard deviation Θ (17). Inhomogeneous broadening causes both the absorption spectrum and Raman excitation profiles to lose vibronic structure, but it does not change the integrated intensity of either, because inhomogeneous effects enter the calculation as a normalized distribution at the probability level.

Because a number of the Raman-active modes in rhodopsin have frequencies $\leq kT$, we also need to include the broadening due to molecules whose initial state is vibrationally excited. The four modes below 300 cm^{-1} are significantly ($\geq$1%) populated to $i = 2$ at 277°K. The required Raman and absorption overlaps for these thermally excited states are easily calculated using the linear excited-state model described in reference 18. The expressions for $\langle 0|0(t)\rangle$ and $\langle 1|0(t)\rangle$ have been given earlier (18). The derived expressions for the single-mode time-dependent overlaps, $\langle i|i(t)\rangle$ and $\langle f|i(t)\rangle$, when $i = 1$ or 2 are (30):

$$\langle 0|0(t)\rangle = \left(\frac{2}{2+i\omega t}\right)^{1/2} \exp\left[\frac{-\beta^2 t^2}{24\hbar^2}(6+i\omega t)\right] \quad (5)$$

[2]The multimode Boltzmann factor for each initial state is found by multiplying together the normalized, single-mode Boltzmann factors. The normalized Boltzmann factor for mode m in vibrational level i is found with the formula, $B_{i,m} = \exp[-(i+\frac{1}{2})\hbar\omega/kT]/\Sigma_{i=0}^{2}\exp[-(i+\frac{1}{2})\hbar\omega/kT]$ where ω is the ground-state frequency of mode m and T is the temperature.

$$\langle 1|0(t)\rangle = \frac{-i\beta t}{\hbar\sqrt{2}}\langle 0|0(t)\rangle \quad (6)$$

$$\langle 1|1(t)\rangle = \left[\frac{2}{2+i\omega t} - \frac{\beta^2 t^2}{2\hbar^2}\right]\langle 0|0(t)\rangle \quad (7)$$

$$\langle 2|1(t)\rangle = \frac{i\beta t}{\hbar}\left[\frac{\beta^2 t^2}{4\hbar^2} - \frac{4+i\omega t}{2(2+i\omega t)}\right]\langle 0|0(t)\rangle \quad (8)$$

$$\langle 2|2(t)\rangle = \left[\frac{\beta^4 t^4}{4\hbar^4} - \frac{\beta^2 t^2}{\hbar^2}\left(\frac{4+i\omega t}{2+i\omega t}\right) + \frac{8-\omega^2 t^2}{(2+i\omega t)^2}\right]\frac{\langle 0|0(t)\rangle}{2} \quad (9)$$

$$\langle 3|2(t)\rangle = \frac{-i\beta t}{\hbar\sqrt{6}}\left[\frac{\beta^4 t^4}{8\hbar^4} - \frac{\beta^2 t^2}{\hbar^2}\left(\frac{3+i\omega t}{2+i\omega t}\right) + \frac{6}{(2+i\omega t)^2} + \frac{3}{2}\right]\langle 0|0(t)\rangle. \quad (10)$$

In these expressions $\beta/\hbar$ is the slope of the excited-state potential surface and ω is the ground-state frequency. The single-mode overlaps which initiate from higher-lying ground-state vibrational levels evolve much faster at short times than the corresponding $i = 0$ overlaps due to the presence of more nodes in the overlapping wavefunctions. When the Raman-active mode is thermally excited, the calculated Raman scattering will be more intense because the single-mode $\langle f|i(t)\rangle$ rises to a maximum much faster, before other homogeneous damping effects become significant. When other modes are thermally excited, the faster fall-off of their $\langle i|i(t)\rangle$'s will damp the multimode $\langle f|i(t)\rangle$ more rapidly, resulting in weaker Raman scattering. The ensemble-averaged cross-sections depend on an interplay of these two effects which is sensitive to temperature, mode frequencies, and the excited-state slopes.

We initially assumed that the cross-sections at 514.5 nm are proportional to Δ^2 and used these deltas referenced to $\Delta_{1549} = 1.0$ as a starting point in the analysis. The 25 observed modes were used in the time-dependent calculations and the other parameters were selected to best model the experimental absorption spectrum and excitation profiles. The scaling of the deltas is determined by the width of the absorption band. The homogeneous width is determined by the magnitude of the absolute resonance Raman cross-sections and the shape of the absorption spectrum on the red edge. The transition moment (M) is dictated by the magnitude of the absorption cross-section. Finally, the degree of inhomogeneous broadening (Θ) and the energy gap between the ground and excited potential surfaces (E_0) are chosen to give the correct absorption band-shape and position. This process is iterated several times until the experimental and calculated excitation profiles and absorption spectra are in agreement. The parameters could not be altered by more than ±5% without significantly reducing the goodness of fit.

RESULTS

The resonance Raman spectra of rhodopsin are shown in Fig. 3 and the cross-sections are summarized in Table I. The symmetric stretch of nitrate, the intensity standard used in these spectra, is seen at 1,049 cm^{-1}. Previous studies have suggested that extensive progressions in low-frequency modes may contribute significantly to the overall absorption lineshape (18, 31, 32). Therefore, we measured the low-frequency spectrum of rhodopsin (Fig. 4 *A*) and observed five lines at 336, 461, 809, 824, and 859 cm^{-1}. However, these modes have insufficient Raman

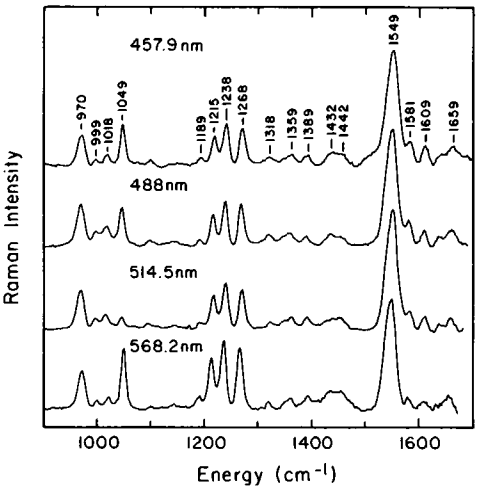

FIGURE 3 Resonance Raman spectra of rhodopsin. Rhodopsin and KNO_3 concentrations are 21 μM and 0.23 M for 457.9 nm, 26 μM and 0.47 M for 488 nm, 21 μM and 0.18 M for 514.5 nm, and 21 μM and 0.41 M for 568 nm excitation. Each resonance Raman spectrum has been divided by a tungsten-halogen lamp spectrum (Eppley Laboratory Inc., Newport, RI) to correct for detection sensitivity. The 1,049 cm^{-1} line is due to NO_3^-.

intensity to contribute substantially to the absorption lineshape. To reach lower wavenumbers, we used the photon-counting Raman system because of its better stray light rejection. Four intense lines were found at 98, 135, 249, and 262 cm^{-1} whose intensities were determined by reference to the intensity of the 970 cm^{-1} line, measured at the same time. These four lines were absent in the bleached spectrum taken immediately after the experiment under identical conditions. Thus, we conclude that these features are chromophore lines and not spurious Rayleigh features or protein lines. These lines are very intense, having cross-sections of the same magnitude as the single-bond stretches (see Table I). These modes will therefore make a major contribution to the absorption lineshape. INDO and QCFF/PI calculations on the 11-*cis*-retinal chromophore (31, 32) and vibrational assignments of conjugated polyenes (33) indicate that single- and double-bond torsions are found in this region of the Raman spectrum. We therefore ascribe the modes at 98, 135, 249, 262, 336, and 461 cm^{-1} to torsional modes.

Fig. 5 demonstrates the good agreement between the experimental Raman excitation profiles and absorption spectra and those calculated using the parameters of Table I. Similarities in the relative intensities at different excitation wavelengths indicate that the enhancement profiles of these modes should be similar and this is borne out in the calculations. The calculated and experimental absorption spectra and excitation profiles are broad and featureless, suggesting rapid dynamics in the excited-state and/or large inhomogeneous effects. Attempts to model these data using a Lorentzian lineshape function whose width was large enough to give the correct Raman cross-sections were unsuccessful because they predicted a large red-edge tail

TABLE I
ABSOLUTE RESONANCE RAMAN CROSS-SECTIONS OF RHODOPSIN

Mode	$\|\Delta\|$	Excitation wavelength (nm)				
		457.9	488.0	514.5	568.2	647.1
98	80 (0.82)*	—/23	—/57	62/79	—/24	—/0.2
135	225 (1.67)*	—/164	—/401	447/552	—/174	—/1
249	174 (0.70)*	—/82	—/199	316/273	—/84	—/0.6
262	231 (0.88)*	—/137	—/330	425/455	—/143	—/1
336	127 (0.38)*	—/35	68/82	—/115	—/34	—/0.2
461	111 (0.24)*	—/26	53/62	—/85	—/25	—/0.2
809	0.14	—/23	36/39	—/52	—/10	—/0.1
824	0.16	—/31	50/52	—/69	—/13	—/0.1
859	0.14	—/25	42/42	—/55	—/11	—/0.1
970	0.50	313/378	448/587	836/777	182/146	—/2
999	0.14	32/31	53/47	76/62	12/12	—/0.1
1018	0.32	137/164	251/249	417/330	58/61	—/0.7
1189	0.14	50/38	54/54	40/70	—/13	—/0.2
1215	0.35	231/243	307/347	446/442	124/79	—/1
1238	0.40	309/325	383/462	565/583	142/104	—/1
1268	0.38	290/303	354/428	524/534	122/95	—/1
1318	0.22	150/107	99/150	291/183	10/32	—/0.4
1359	0.20	104/93	149/129	137/154	20/27	—/0.4
1389	0.18	90/78	82/108	157/126	38/22	—/0.3
1432	0.24	174/140	95/194	255/220	27/38	—/0.6
1442	0.25	202/154	78/213	305/240	51/41	—/0.6
1549	0.87	2170/2209	2510/3038	3180/3144	604/524	33/8
1581	0.22	115/147	269/202	151/203	43/34	—/0.5
1609	0.29	154/269	375/368	443/362	37/60	—/1
1659	0.27	251/249	279/338	290/319	—/52	—/0.8

The data are shown as experimental/calculated cross-sections in units of $Å^2$/molecule $\times 10^{10}$. Uncertainties in intensities relative to nitrate are ~10% for strong lines and ~20% for weak lines. The conversion to absolute cross-sections introduces a further uncertainty estimated at 10%, principally from the nitrate cross-sections. Δ's are in units of dimensionless normal coordinates. The dimensionless coordinate, q, is related to the Cartesian coordinate, x, by $q = (\mu\omega/\hbar)^{1/2} x$, where μ is the reduced mass. The calculations used $E_0 = 18{,}500\ cm^{-1}$, transition length $M = 2.079$ Å, temperature $T = 277°K$, Gaussian homogeneous linewidth $\Gamma_{Gauss} = 170\ cm^{-1}$ half-width, and inhomogeneous linewidth $\Theta = 910\ cm^{-1}$ half-width. Thermally excited initial states to $i = 2$ were considered in modes below $300\ cm^{-1}$. *For these lines, the calculation was performed using the linear excited-state model. The excited-state slope of $\beta/\hbar$ is given in units of cm^{-1} and the number in parentheses gives the equivalent harmonic surface displacement calculated using $\beta/\hbar = \Delta\omega$.

on the absorption that is inconsistent with experiment. This forced us to use a Gaussian homogeneous lineshape.

Examination of the Raman cross-sections and the Raman overlaps $\langle f|i(t)\rangle$ clearly illustrate the role of torsional deformations and the Gaussian homogeneous decay in the overall molecular dynamics. In Fig. 6 *A* the resonance Raman excitation profile for the 970 cm^{-1} mode has been calculated under a variety of conditions. The dotted lines demonstrate that the Gaussian half-width is fairly precisely defined ($\pm 50\ cm^{-1}$) by the fit to the Raman cross-sections. If Γ is $<120\ cm^{-1}$, the calculated cross-sections are significantly above the experimental values. The excitation profiles have also been calculated with and without the torsional modes and the Gaussian decay. With the torsional modes and the Gaussian decay removed, the calculated cross-sections are ~20-fold too large (*solid line*). In Fig. 6 *B* it is clear that the area under the multimode $\langle f|i(t)\rangle$, which is proportional to the Raman cross-section, is strongly reduced when the torsions are included because the Raman overlap must be multiplied by a rapidly decaying torsional $\langle i|i(t)\rangle$ (*dotted line*). However, even with all the torsional degrees of freedom included, the calculated cross-sections are still a factor of 1.5 too high. Thus, the cross-sections require the inclusion of a rapidly decaying homogeneous lineshape function ($t_{1/2} = 45$ fs). In summary, the damped resonance Raman cross-sections require that $\langle f|i(t)\rangle$ must decay rapidly and permanently. The rapid decay at short times is due to large torsional distortion of the chromophore after electronic excitation. The permanence of the decay of $\langle f|i(t)\rangle$ is ensured by the Gaussian homogeneous decay whose origin will be discussed.

The contributions of the inhomogeneous width, thermal populations of low frequency modes, the Gaussian homogeneous width, and the torsional progressions to the absorption bandshape of rhodopsin are shown in Fig. 7. Spectrum *A* was calculated using the parameters in Table I. *B* presents the absorption spectrum with the inhomogeneous width Θ and the temperature set to zero. The appearance of broad 0←0, 1←0, and 2←0 bands clearly shows that the inhomogeneous broadening (910 cm^{-1} half-width) and thermal broadening contribute significantly to the diffuseness. Spectrum *C* was calculated by also setting the Gaussian decay Γ to zero, whereas in *D* the low-frequency

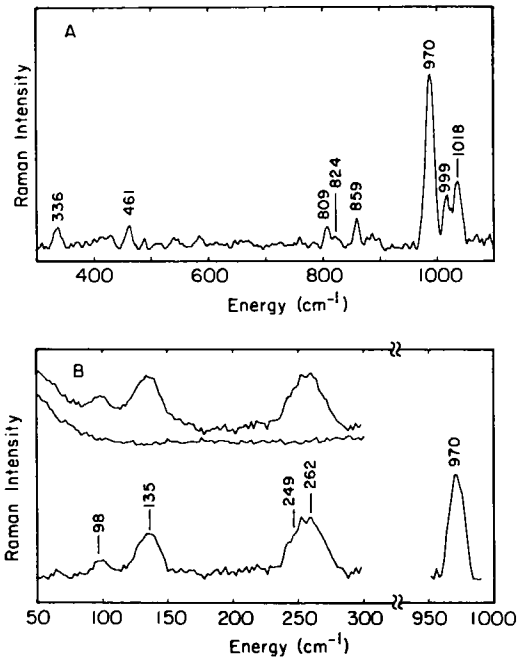

FIGURE 4 Low frequency Raman spectra of rhodopsin. Spectrum *A* is the sum of four scans of a 25-μM rhodopsin solution exciting at 488 nm obtained on the multichannel system and treated as described in the text. The top spectrum shown in *B* is the sum of three scans obtained on the single-channel, double monochromator system exciting at 514.5 nm. The middle spectrum is the sum of three bleached scans obtained using the same conditions. The bottom spectrum gives the difference with a subtraction factor (1.4) chosen to give the best flat background. In addition, a broad feature from 50–150 cm^{-1} was removed using a cubic spline fitting routine. Thus, the residual scattering is, if anything, an underestimate. The cross-sections of the four lines at 98, 135, 249, and 262 cm^{-1} were determined by referencing to the 970-cm^{-1} line which was measured in the same experiment (*inset*).

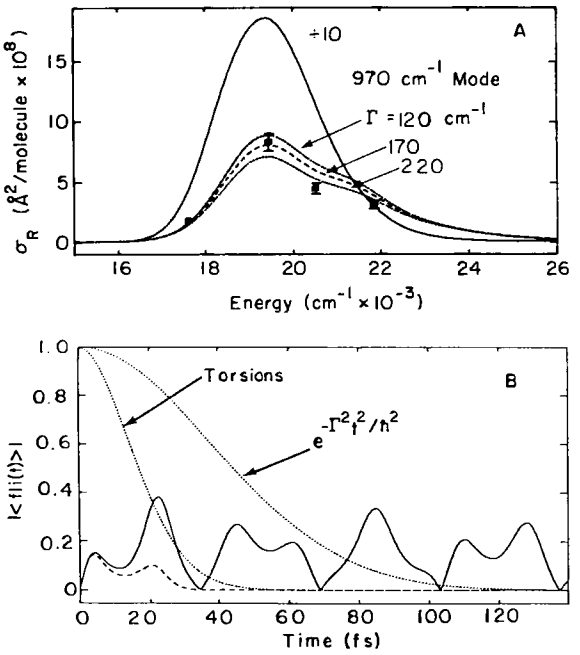

FIGURE 6 Effect of low-frequency torsional modes and the Gaussian homogeneous decay on the resonance Raman excitation profiles (*A*) and Raman overlap (*B*) for the 970 cm^{-1} mode. The dashed lines in *A* and *B* were calculated using the parameters of Table I. The solid lines in *A* and *B* were calculated after the removal of all low-frequency torsional modes (<500 cm^{-1}) and the Gaussian homogeneous decay. The dotted lines in *A* illustrate the sensitivity of the final synthesis to alteration of the Gaussian homogeneous width. The dotted lines in *B* present $\langle i|i(t)\rangle$ for the six low-frequency torsional modes and the 45-fs Gaussian decay.

modes were also removed. Comparison of curves *C* and *D* shows that torsional progressions make a significant contribution to the homogeneous absorption bandshape, in agreement with the predictions of Birge et al. (31) and Warshel and Karplus (32). It is also evident that the overall width of the absorption band is determined by

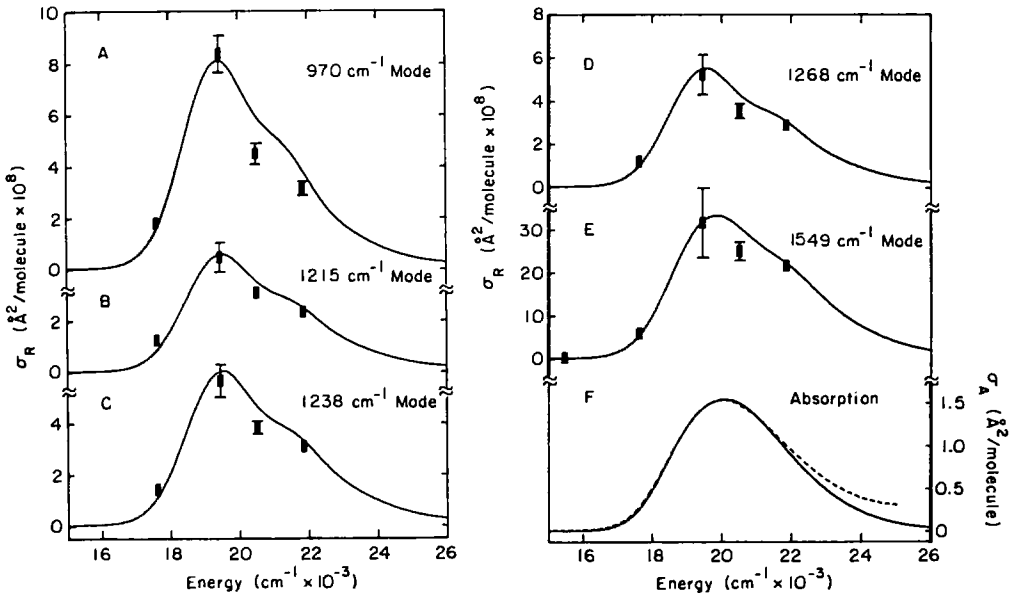

FIGURE 5 Experimental (points) and calculated resonance Raman excitation profiles and absorption spectra for rhodopsin. The experimental absorption is indicated by a dashed line. The solid line is generated by the final parameters of Table I. Error bars represent the uncertainties in the absolute cross-sections. Deviations of the calculated spectrum from the experimental absorption spectrum at ~24,000 cm^{-1} are most likely due to the presence of one or more higher-lying electronic states.

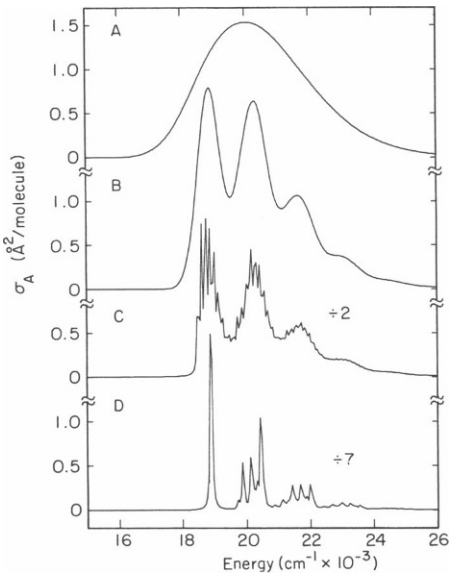

FIGURE 7 Contribution of various broadening mechanisms to the absorption bandshape of rhodopsin. *A* is calculated using the parameters of Table I. *B* is calculated with the inhomogeneous width Θ and temperature set to zero. *C* is calculated with the inhomogeneous width, temperature, and Gaussian homogeneous width set to zero. *D* is calculated with the additional removal of all low-frequency modes (<500 cm^{-1}). To make the calculation tractable, a Lorentzian homogeneous linewidth (Γ = 13 cm^{-1} half-width) has been included in the calculations of spectra *C* and *D*. The zero–zero energy in *D* has been adjusted to compensate for changes in the zero-point energy caused by the removal of the torsions.

progressions in high-frequency modes with the 1,549 cm^{-1} ethylenic stretch as the major contributor.

DISCUSSION

The primary purpose of this study is to examine the dynamics of the excited-state isomerization of the retinal chromophore in rhodopsin. The following temporal picture is suggested by these data. After excitation, the wavepacket leaves the Franck-Condon region rapidly along high-frequency single- and double-bond stretching modes. By the time it returns to the Franck-Condon region along these high-frequency modes (~20 fs), the molecule has distorted significantly about low-frequency torsional modes such that the multimode overlap $\langle i|i(t)\rangle$ is strongly damped. At longer times (>200 fs), strong radiationless coupling (surface crossing) associated with isomerization must occur that damps out any later recurrences. The strong coupling is represented in this study by dissociative torsions and the Gaussian homogeneous decay. This picture is consistent with subpicosecond absorption studies on bacteriorhodopsin which indicate that the torsional distortion of the retinal chromophore occurs on a 100–150–fs timescale (34) and that electronic relaxation occurs with a $t_{1/2}$ of ~500 fs (34, 35).

The observation of explicit low-frequency torsional modes at 98, 135, 249, 262, 336, and 461 cm^{-1} is an intriguing result of this study. By modeling the excited-state potential of the C_{11}=C_{12} torsion as a linear surface, the intensities of these modes can be used to make a rough estimate of the torsional isomerization time. QCFF/PI calculations predict that the C_{11}=C_{12} torsion is primarily localized in a mode at 537 cm^{-1}. Therefore, we will assume that the Raman line at 461 cm^{-1} can be assigned as this torsion. If a wavepacket is propagated on the linear excited-state surface of the 461 cm^{-1} mode, it will reach a dimensionless coordinate of 11, corresponding to a torsional angle of 90°, in only 100 fs (19). This suggests that the isomerization could occur as fast as 0.2 ps. Because modes below 300 cm^{-1} have very large excited-state slopes, even larger single-bond torsions and skeletal deformations in addition to the C_{11}=C_{12} torsion occur during the isomerization. Normal mode assignments of these lines will provide specific projections of these modes on the isomerization coordinate and introduce further constraints in models of the isomerization mechanism.

The Gaussian homogeneous linewidth used in this study requires comment. The decay of the Gaussian is too fast to be purely electronic relaxation; other studies have shown 500 fs to be a reasonable electronic relaxation time for rhodopsins (34, 35). One possibility is that the Gaussian decay is due to distortions along torsional modes which are too low in frequency to be observed in this study. Modes below ~50 cm^{-1} are very difficult to observe experimentally even if they are highly displaced. It seems more likely, however, that the Gaussian decay arises from rapid dephasing. As the polyene torsionally distorts, the excited electronic-state character will change very dramatically, producing concomitant changes in the vibrational potential surfaces. Because of the obvious Born-Oppenheimer breakdown, this process should be thought of as "vibronic dephasing."

A previous INDO calculation of isomerization trajectories has predicted that rhodopsin distorts along a barrierless C_{11}=C_{12} torsional coordinate on the excited-state potential surface to a 90° twisted geometry from which it crosses to the ground-state potential surface and forms either rhodopsin or bathorhodopsin (13). Similarly, in our model the wavepacket propagates along low-frequency modes on the excited-state surface until it reaches a geometry where electronic relaxation to the ground-state potential surface is optimized. Our predicted time to a 90° twisted geometry (~100 fs) is in good agreement with picosecond fluorescence experiments which suggest 80–170 fs and with recent measurements on bacteriorhodopsin (bR) (12, 34). However, INDO calculations (13) predict times of 800–1,100 fs to reach the 90° geometry, suggesting that the theoretical excited-state slopes are low.

The two largest geometry changes occur in the 1,549 cm^{-1} ethylenic stretch and 970 cm^{-1} 11,12 hydrogen-out-of-plane (HOOP) lines. The large delta in the 1,549 cm^{-1} ethylenic stretch quantitates the change in double-bond strength in the excited-state. The large delta in the 970 cm^{-1} HOOP mode has been interpreted in terms of

ground-state distortions about the C_{10}—C_{11}, C_{11}=C_{12}, and C_{12}—C_{13} bonds that allow this mode to acquire resonance Raman intensity (4, 5, 14). A HOOP mode with a delta of 1.2 has also been seen at 963 cm^{-1} in *cis*-stilbene, which is distorted around the exocyclic double bond in the ground state (19). These ground-state distortions have led to the appealing suggestion that the retinal chromophore is twisted around the C_{11}=C_{12} double bond in such a way that the isomerization process is "primed" (22). This may help to account for the unusually short time (9–13) required for this isomerization and may contribute to the high quantum yield for isomerization (ϕ_{isom} = 0.67, reference 36).

We have previously determined the excited-state structure and dynamics of the bR chromophore from resonance Raman intensities (17, 18). The most interesting similarities between rhodopsin and bR occur in the calculated excited-state relaxation times for the two proteins. The analysis of rhodopsin is essentially identical to that of bR, except that in bR no low-frequency modes with significant resonance Raman intensity have thus far been detected. Therefore, a Gaussian homogeneous damping function which represented distortion on a highly displaced torsional surface had to be included to account for the damped Raman cross-sections and broad absorption bandshape. The wavepacket leaves the Franck-Condon region very rapidly in both bR and rhodopsin; $\langle i|i(t)\rangle$ decays to zero in 30 and 35 fs, respectively. Thus, the excited-state relaxation in each is similar. Since both molecules undergo double-bond isomerizations in a protein, this suggests that the mechanism for isomerization is analogous. An additional similarity is the relatively large amount of inhomogeneous broadening required in the calculations for bR (Θ = 560 cm^{-1}, half-width) and rhodopsin (Θ = 910 cm^{-1}, half-width) to account for the spectral diffuseness. This inhomogeneous width could be due to differences in protein-chromophore interactions associated with the opsin shift.

CONCLUSIONS

Resonance Raman intensities have been used to perform a complete Franck-Condon analysis of the absorption bandshape in the visual pigment rhodopsin. The majority of the absorption spectral width is due to Franck-Condon progressions in high-frequency ethylenic stretching modes. Low-frequency torsional modes and the Gaussian homogeneous linewidth contribute to the diffuseness of the absorption spectrum and are responsible for the reduced Raman cross-sections. Inhomogeneous site distribution effects also make a large contribution to the absorption bandshape. The excited-state geometry changes determined in this study can now be used to critically evaluate theoretical calculations of the mechanism of excited-state photoisomerization. Also, now that the factors which contribute to the absorption width and lineshape have been identified, it should be possible to more quantitatively analyze wavelength-dependent trends in visual pigment absorption linewidths and lineshapes.

We thank Ilona Palings and Kim Friedlander for helping in the preparation of rhodopsin samples, and Anne Myers, Tom Pollard, and Mark Trulson for illuminating discussions.

This work was supported by grants from the National Institutes of Health (EY 02051) and the National Science Foundation (CHE 86-15093).

Received for publication 1 September 1987 and in final form 7 March 1988.

REFERENCES

1. Birge, R. 1981. Photophysics of light transduction in rhodopsin and bacteriorhodopsin. *Annu. Rev. Biophys. Bioeng.* 10:315–354.
2. Yoshizawa, T., and G. Wald. 1963. Pre-lumirhodopsin and the bleaching of visual pigments. *Nature (Lond.).* 197:1279–1286.
3. Oseroff, A. R., and R. H. Callender. 1974. Resonance Raman spectroscopy of rhodopsin in retinal disk membranes. *Biochemistry.* 13:4243–4248.
4. Eyring, G., B. Curry, R. Mathies, R. Fransen, I. Palings, and J. Lugtenburg. 1980. Interpretation of the resonance Raman spectrum of bathorhodopsin based on visual pigment analogues. *Biochemistry.* 19:2410–2418.
5. Eyring, G., B. Curry, A. Broek, J. Lugtenburg, and R. Mathies. 1982. Assignment and interpretation of hydrogen out-of-plane vibrations in the resonance Raman spectra of rhodopsin and bathorhodopsin. *Biochemistry.* 21:384–393.
6. Siebert, F., W. Mantele, and K. Gerwert. 1983. Fourier transform infrared spectroscopy applied to rhodopsin: the problem of the protonation state of the retinylidene Schiff base re-investigated. *Eur. J. Biochem.* 136:119–127.
7. Rothschild, K. J., W. A. Cantore, and H. Marrero. 1983. Fourier transform infrared difference spectra of intermediates in rhodopsin bleaching. *Science (Wash. DC).* 219:1333–1335.
8. Bagley, K. A., V. Balogh-Nair, A. A. Croteau, G. Dollinger, T. G. Ebrey, L. Eisenstein, M. K. Hong, K. Nakanishi, and J. Vittitow. 1985. Fourier transform infrared difference spectroscopy of rhodopsin and its photoproducts at low temperature. *Biochemistry.* 24:6055–6071.
9. Busch, G. E., M. L. Applebury, A. A. Lamola, and P. M. Rentzepis. 1972. Formation and decay of prelumirhodopsin at room temperatures. *Proc. Natl. Acad. Sci. USA.* 69:2802–2806.
10. Peters, K., M. L. Applebury, and P. M. Rentzepis. 1977. Primary photochemical event in vision: proton translocation. *Proc. Natl. Acad. Sci. USA.* 74:3119–3123.
11. Hayward, G., W. Carlsen, A. Siegman, and L. Stryer. 1981. Retinal chromophore of rhodopsin photoisomerizes within picoseconds. *Science (Wash. DC).* 211:942–944.
12. Doukas, A. G., M. R. Junnarkar, R. R. Alfano, R. H. Callender, T. Kakitani, and B. Honig. 1984. Fluorescence quantum yield of visual pigments: evidence for subpicosecond isomerization rates. *Proc. Natl. Acad. Sci. USA* 81:4790–4794.
13. Birge, R., and L. Hubbard. 1980. Molecular dynamics of cis-trans isomerization in rhodopsin. *J. Am. Chem. Soc.* 102:2195–2205.
14. Warshel, A., and N. Barboy. 1982. Energy storage and reaction pathways in the first step of the vision process. *J. Am. Chem. Soc.* 104:1469–1476.
15. Honig, B., T. Ebrey, R. H. Callender, U. Dinur, and M. Ottolenghi. 1979. Photoisomerization, energy storage, and charge separation: a model for light energy transduction in visual pigments and bacteriorhodopsin. *Proc. Natl. Acad. Sci. USA.* 76:2503–2507.
16. Liu, R., and A. E. Asato. 1985. The primary process of vision and the structure of bathorhodopsin: a mechanism for photoisomerization of polyenes. *Proc. Natl. Acad. Sci. USA.* 82:259–263.
17. Myers, A. B., and R. A. Mathies. 1987. Resonance Raman intensi-

ties: a probe of excited state structure and dynamics. *In* Biological Applications of Raman Spectroscopy. Vol 2. Resonance Raman Spectra of Polyenes and Aromatics. T. G. Spiro, editor. Wiley-Interscience, New York. 1–58.

18. Myers, A. B., R. A. Harris, and R. A. Mathies. 1983. Resonance Raman excitation profiles of bacteriorhodopsin. *J. Chem. Phys.* 79:603–613.
19. Myers, A. B., and R. A. Mathies. 1984. Excited-state torsional dynamics of *cis*-stilbene from resonance Raman intensities. *J. Chem. Phys.* 81:1552–1558.
20. Schomaker, K. T., and P. M. Champion. 1986. Investigations of spectral broadening mechanisms in biomolecules: cytochrome *c*. *J. Chem. Phys.* 84:5314–5325.
21. Tsuboi, M., Y. Nishimura, A. Y. Hirakawa, and W. Peticolas. 1987. Resonance Raman spectroscopy and normal modes of the nucleic acid bases. *In* Biological Applications of Raman Spectroscopy. Vol. 2. Resonance Raman Spectra of Polyenes and Aromatics. T. G. Spiro, editor. Wiley-Interscience, New York. 109–179.
22. Palings, I., J. A. Pardoen, E. van den Berg, C. Winkel, J. Lugtenburg, and R. A. Mathies. 1987. Assignment of fingerprint vibrations in the resonance Raman spectra of rhodopsin, isorhodopsin, and bathorhodopsin: implications for chromophore structure and environment. *Biochemistry.* 26:2544–2556.
23. Mathies, R. A., A. R. Oseroff, and L. Stryer. 1976. Rapid-flow resonance Raman spectroscopy of photolabile molecules: rhodopsin and isorhodopsin. *Proc. Natl. Acad. Sci. USA.* 73:1–5.
24. Kato, Y., and H. Takuma. 1971. Experimental study on the wavelength dependence of the Raman scattering cross sections. *J. Chem. Phys.* 54:5398–5402.
25. Schomacker, K. T., J. K. Delaney, and P. M. Champion. 1986. Measurements of the absolute Raman cross-sections of benzene. *J. Chem. Phys.* 85:4240–4247.
26. Dudik, J. M., C. R. Johnson, and S. A. Asher. 1985. Wavelength dependence of the preresonance Raman cross sections of CH_3CN, SO_4^{-2}, ClO_4^- and NO_3^-. *J. Chem. Phys.* 82:1732–1740.
27. Albrecht, A. C., and M. C. Hutley. 1971. On the dependence of vibrational Raman intensity on the wavelength of incident light. *J. Chem. Phys.* 55:4438–4443.
28. Lee, S.-Y., and E. J. Heller. 1979. Time-dependent theory of Raman scattering. *J. Chem. Phys.* 71:4777–4788.
29. Myers, A., R. Mathies, D. J. Tannor, and E. J. Heller. 1982. Excited state geometry changes from preresonance Raman intensities: isoprene and hexatriene. *J. Chem. Phys.* 77:3857–3866.
30. Loppnow, G. R. University of California at Berkeley. Ph.D. thesis. In preparation.
31. Birge, R. R., D. F. Bocian, and L. M. Hubbard. 1982. Origins of inhomogeneous broadening in the vibronic spectra of visual chromophores and visual pigments. *J. Am. Chem. Soc.* 104:1196–1207.
32. Warshel, A., and M. Karplus. 1974. Calculation of $\pi\pi^*$ excited state conformations and vibronic structure of retinal and related molecules. *J. Am. Chem. Soc.* 96:5677–5689.
33. Hudson, B. S., B. E. Kohler, and K. Schulten. 1982. Linear polyene electronic structure and potential surfaces. *In* Excited States. Vol. 6. E. C. Lim, editor. Academic Press, New York. 1–95.
34. Mathies, R. A., C. H. Brito Cruz, W. T. Pollard, and C. V. Shank. 1988. Direct observation of the excited-state *cis-trans* isomerization in bacteriorhodopsin. *Science (Wash. DC).* In press.
35. Polland, H.-J., M. A. Franz, W. Zinth, W. Kaiser, E. Kolling, and D. Oesterhelt. 1986. Early picosecond events in the photocycle of bacteriorhodopsin. *Biophys. J.* 49:651–662.
36. Dartnall, H. J. 1972. Photosensitivity. *In* Handbook of Sensory Physiology. Vol. VII/I. H. J. Dartnall, editor. Springer-Verlag, New York. 122–145.